

# Three Dimensional Wave Scattering by Rigid Circular Pipelines Submerged in an Acoustic Waveguide

António Tadeu, Andreia Pereira, Luís Godinho<sup>1</sup>

**Abstract:** The Boundary Element Method (BEM) is used to compute the three-dimensional variation pressure field generated by a point pressure source inside a flat waveguide channel filled with a homogeneous fluid, in the presence of infinite rigid circular pipelines. The problem is solved in the frequency domain, using boundary elements to model the pipeline and an appropriate Green's function to simulate the free surface and the rigid floor of the channel. Because of the  $2 - 1/2 - D$  geometry of the problem, the separation of variables has been used, and the solution at each frequency is expressed in terms of waves with the varying wavenumber,  $k_z$ . Time responses at different points in the space domain are computed by applying an inverse (Fast) Fourier Transform, using a Ricker pulse as the dynamic excitation source.

Simulation analyses using this idealized model are then used to study the patterns of wave propagation in the vicinity of these inclusions, following waves with different apparent wave velocities along the  $z$  axis. The amplitude of the wavefield in the frequency vs. axial-wavenumber domain is presented, allowing the position of the inclusions to be recognized and identified, providing a basis for the development of non-destructive testing and imaging methods.

**keyword:** wave propagation, seismic prospecting, acoustic mediums

## 1 Introduction

The measurement of spatial and temporal variations, recorded at receivers or geophones and resulting from the generation of seismic waves produced by dynamic sources, placed inside elastic or acoustic media is frequently used to draw inferences on the geological structure of the medium [Özdoğan(1987); Claerbout(1976);

Cordier(1985); Godkin(1985); Griffiths & King(1981)]. The field scattering arises from the interaction of the incident field and inclusions, but it is strongly influenced by the arrangement of the different strata of the earth's crust. The intervals, amplitudes and phase distortions of the waves recorded on the receivers can be used to draw inferences on the geological structure of the medium.

This study analyses the alteration of the amplitude and phase distortion in the pressure field generated by a point pressure source inside a hydraulic waveguide in the presence of rigid pipelines. The BEM is used to solve the problem. The technique is similar to the one already used by the authors [Tadeu and Godinho(1999)] to evaluate the wave-field elicited by a point pressure source in the presence of fixed cylindrical cavities, with irregular cross sections, submerged in an unbounded fluid medium and in a half-space, although here, the Green's functions are obtained by superposing virtual acoustic sources placed in such a way as to generate the free and rigid surfaces of the fluid channel.

Other methods have been used to analyze acoustic scattering from surfaces or compact inclusions submerged inside a fluid waveguide channel. Dawson(1990) formulated a boundary integral equation method to compute the scattering of underwater sound from the compact deformations of an oceanic waveguide's surface. His numerical examples assume that the fluid filling the waveguide has constant density and sound speed. The solution involves a Green's function appropriate to the waveguide in the absence of the boundary deformation, allowing the sound speed to vary with depth. This Green's function is obtained either by taking the Fourier transform of the standard three-dimensional modal expansion [Ahluwalia and Keller(1977)] with respect to a transverse coordinate, or by assuming a vertical eigenfunction expansion for the Green's function and evaluating the coefficients in a manner analogous to the three-dimensional model. The same method was used [Fawcett(1996a), (1996b)] to ob-

<sup>1</sup>Department of Civil Engineering, University of Coimbra, 3030 Coimbra, Portugal

tain the two-dimensional acoustic scattered field generated by objects embedded between two half spaces with different densities.

The boundary element method (BEM) is possibly the best way to analyze wave propagation problems in unbounded media, because it automatically satisfies the far field radiation conditions and allows a compact description of the medium in terms of boundary elements at the material discontinuities alone. In the present paper, we compute the wavefield and motions elicited by monopole sources inside a fluid waveguide, in the presence of circular rigid pipelines, whose geometry in one direction ( $z$ ) does not change. Because of the cylindrical geometry of this problem, we can use the separation of variables and express the solution at each frequency in terms of waves with varying wavenumber,  $k_z$  (with  $z$  being the borehole axis), which we subsequently Fourier-transform into the spatial domain [Tadeu and Godinho(1999)].

The article is organized as follows: first, a brief definition of the 3D problem is given, and then the BEM is formulated in the frequency domain, indicating the required Green's functions. The Boundary Element Method (BEM) is then used to compute the three-dimensional pressure field generated by a point pressure source in the vicinity of an infinite rigid pipeline, submerged in a flat waveguide channel filled with a homogeneous fluid. This model is further used for simulation analyses to investigate wave propagation in the vicinity of such inclusions in the presence of a second cylindrical circular cavity, whose size may vary. Results are obtained in the frequency and in the time domains, in particular for different apparent wave velocities along the  $z$  axis, to quantitatively study the 3D effects of the scattering. A large number of simulations was performed to study how different parameters, such as the size of the inclusions, affect the three-dimensional scattering wave patterns.

## 2 Problem statement

Consider a cylindrical irregular inclusion of infinite extent, submerged in a spatially uniform fluid medium, subjected to a harmonic point pressure load at position  $(x_0, 0, 0)$ , oscillating with a frequency  $\omega$ .

$$p_{inc} = \frac{Ae^{i\frac{\omega}{\alpha}(t - \sqrt{(x-x_0)^2 + y^2 + z^2})}}{\sqrt{(x-x_0)^2 + y^2 + z^2}} \quad (1)$$

in which the subscript *inc* denotes the incident field,  $A$  is the wave amplitude,  $\alpha$  is the pressure wave velocity of the medium, and  $i = \sqrt{-1}$ .

Defining the effective wavenumbers

$$k_\alpha = \sqrt{\frac{\omega^2}{\alpha^2} - k_z^2}, \quad \text{Im}k_\alpha < 0 \quad (2)$$

by means of the axial wavenumber  $k_z$ , and Fourier-transforming Eq.1 in the  $z$  direction, one obtains

$$\hat{p}_{inc}(x, y, k_z, \omega) = \frac{-iA}{2} H_0^{(2)} \left( k_\alpha \sqrt{(x-x_0)^2 + y^2} \right) \quad (3)$$

in which the  $H_n^{(2)}(\dots)$  are second Hankel functions of order  $n$ .

If one considers an infinite set of periodically placed sources along the  $z$  direction at equal intervals,  $L$ , the incident field may be written as

$$p_{inc}(\omega, x, y, z) = \frac{2\pi}{L} \sum_{m=-\infty}^{\infty} \hat{p}_{inc}(x, y, k_z, \omega) e^{-ik_z z} \quad (4)$$

with  $k_z = \frac{2\pi}{L}m$ . This equation converges and can be approximated by a finite sum of terms.

The problem to be solved considers a spatially uniform inviscid fluid medium bounded by two flat surfaces, with irregular submerged inclusions. The pressure field defined by Eq.3 needs to be reformulated to satisfy the boundary conditions at the surface and floor. The normal velocity must be null at the flat floor of the channel and at the rigid surface, under ice formations, in cold regions. On the other hand, the pressure reaches null values when the surface is open. This function can be achieved by superposing the pressure field generated by virtual sources with positive or negative polarity, and located so that the desired boundary conditions are ensured [Tadeu(1992)]. In the case of a free surface, the pressure field Green's function  $G(x, x_0, \omega)$  is given by the following expression:

$$G(\underline{x}, \underline{x}_0, \omega) = \frac{-i}{4} [H_0(k_\alpha r)] + \frac{-i}{4} \left\{ \sum_{n=0}^{NS} (-1)^n \left[ H_0(k_\alpha r_1) - \sum_{i=2}^4 H_0(k_\alpha r_i) \right] \right\} \quad (5)$$

and when the surface is rigid it takes the form:

$$G(\underline{x}, \underline{x}_0, \omega) = \frac{-i}{4} [H_0(k_\alpha r)] + \frac{-i}{4} \left\{ \sum_{n=0}^{NS} \left[ \sum_{i=1}^4 H_0(k_\alpha r_i) \right] \right\} \quad (6)$$

in which  $r = \sqrt{(x-x_0)^2 + (y-y_0)^2}$

$$r_1 = \sqrt{(x-x_0)^2 + (y+y_0+2hn)^2}$$

$$r_2 = \sqrt{(x-x_0)^2 + (y-2h-y_0-2hn)^2}$$

$$r_3 = \sqrt{(x-x_0)^2 + (y+2h-y_0+2hn)^2}$$

$$r_4 = \sqrt{(x-x_0)^2 + (y-2h+y_0-2hn)^2}$$

$h$  is the thickness of the channel, and

$\rho$  is the mass density of the fluid medium.

The number of sources used ( $NS$ ) is determined so that all the signals needed to define the signal within the time interval fixed by the frequency increment are taken into account.

### 3 Boundary Element formulation

The Boundary Element Method (BEM) is used to obtain the three-dimensional field generated by the scattering from a cylindrical inclusion with an irregular shape. In the case of an acoustic medium, the  $2 - 1/2 - D$  problem can be solved as a discrete summation of two-dimensional BEM solutions for different  $k_z$  wavenumbers. Then, using the inverse Fourier transform, the  $3D$  field can be synthesized. The wavenumber transform is obtained in discrete form, as explained above, by considering an infinite number of virtual point sources spaced at equal intervals along the  $z$  axis and at a sufficient distance from each other to avoid spatial contamination [Bouchon and Aki(1977)].

Since the literature on the BEM is comprehensive, we do not give full details of the formulation required for the type of scattering problem presented here (see for example, [Manolis & Beskos(1988)]). Next, we present a brief description of the BEM solution required to solve each two-dimensional problem.

For frequency domain analysis, the acoustic pressure ( $p$ ) at any point of the spatial domain can be calculated making use of a single scalar equation, known as the Helmholtz equation,

$$\nabla^2 p_{\underline{x}, \omega} + k_\alpha^2 p(\underline{x}, \omega) = 0 \quad (7)$$

where  $k_\alpha = \sqrt{\frac{\omega^2}{\alpha^2} - k_z^2}$ . Considering a homogeneous fluid medium of infinite extent, containing an inclusion of volume  $V$ , bounded by a surface  $S$ , the boundary integral equations can be constructed by applying the reciprocity

theorem, leading to

$$c p(\underline{x}_0, k_z, \omega) = \int_S q(\underline{x}, \mathbf{v}_n, \omega) G(\underline{x}, \underline{x}_0, k_z, \omega) ds - \int_S H(\underline{x}, \mathbf{v}_n, \underline{x}_0, k_z, \omega) p(\underline{x}, k_z, \omega) ds \quad (8)$$

In this equation  $G$  and  $H$  are respectively the fundamental solutions for the pressure ( $p$ ) and pressure velocity ( $q$ ), at  $\underline{x}$  due to a virtual point load at  $\underline{x}_0$ . The factor  $c$  is a constant defined by the shape of the boundary, receiving the value  $1/2$  if  $\underline{x}_0 \in S$  and is smooth.

The boundary conditions prescribe null normal pressure velocities along the boundary  $S$ . Thus, Eq. 8 is simplified to

$$c p(\underline{x}_0, k_z, \omega) = - \int_S H(\underline{x}, \mathbf{v}_n, \underline{x}_0, k_z, \omega) p(\underline{x}, k_z, \omega) ds \quad (9)$$

Assuming the existence of an incident pressure wavefield striking the boundary, defined by Eq. 5 or Eq. 6, the following equation is derived,

$$c p(\underline{x}_0, k_z, \omega) = - \int_S H(\underline{x}, \mathbf{v}_n, \underline{x}_0, k_z, \omega) p(\underline{x}, k_z, \omega) ds + \hat{p}^{inc}(\underline{x}_0, k_z, \omega) \quad (10)$$

The solution of this integral for an arbitrary boundary surface ( $S$ ) requires the discretization of the boundary into  $N$  straight boundary elements, for which boundary values  $p^k$  are ascribed. For constant value pressure boundary elements, Eq. 10 takes the form,

$$c p^k = - \sum_{l=1}^N H^{kl} p^l + p_{inc}^k \quad (11)$$

with  $H^{kl} = \int_{C_l} H(\underline{x}_l, n_l, \underline{x}_k, k_z, \omega) ds$ , where  $k$  is the loaded element,  $p^l$  is the pressure in element  $l$  and  $H^{kl}$  is the pressure velocity component at  $\underline{x}_l$  due to a pressure load at  $\underline{x}_k$  and  $n_l$  is the outward normal for the  $l^{th}$  boundary segment  $C_l$ . The required pressure velocity function ( $H$ ) is obtained by differentiating Eq.5 and 6 in relation to the unit outward normal.

The application of virtual loads along all boundary nodal points (Eq.11,  $k = 1, N$ ) allows the definition of a linear system of equations that can be solved for the  $N$  nodal pressures.

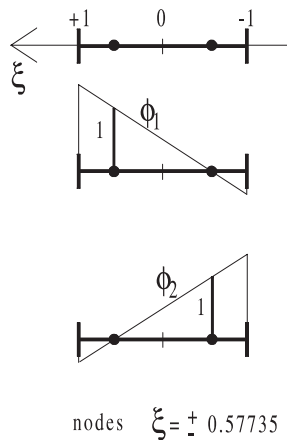


**Figure 1** : Discontinuous linear boundary elements. Interpolating functions and nodal points position.

If the pressure is allowed to vary linearly within the boundary elements, using linear interpolation functions, then the number of nodes to be considered inside each element equals two. Twice the number of equations defined above are required, and the resulting integration then takes the form,

$$H^{kl} = \int_{C_l} \phi H(\underline{x}_l, n_l, \underline{x}_k, k_z, \omega) ds \quad (12)$$

where  $\phi$  represents the required interpolation functions. Fig. 1 illustrates the interpolation functions and the position of the nodal points. Integrations in Eq.12 are performed by means of Gauss-Legendre quadrature, using four integration points.

The scattered pressure field in the fluid is then defined as a function of the nodal pressure values, as follows,

$$p_{sca}^k = \sum_{l=1}^{2N} p^l H^{kl} \quad (13)$$

where  $p_{sca}^k$  is the scattered pressure field at receiver  $k$ ,  $N$  is the total number of boundary elements, and  $p^l$  is the nodal pressure value at element  $l$ .

The BEM algorithm was implemented and validated by applying it to a fixed cylindrical circular cavity, subjected to a harmonic point pressure load applied, for which the solution is known in closed form (see Pao and Mow (1973)). Notice that Eq.5 and 6 were specialized to solve the present BEM problem by setting the  $NS$  parameter to zero.

#### 4 Time domain solution

The pressures in the time domain can be obtained by fast Fourier transform in  $\omega$ , taking the source whose temporal variation is given by a Ricker pulse. Complex frequencies of the form  $\omega_c = \omega - i\eta$  (with  $\eta = 0.7\Delta\omega$ ) have been used to prevent the aliasing phenomena and to minimize the contamination of the response by the periodic virtual sources. In the time domain, this shift is later taken into account by applying an exponential window  $e^{\eta t}$  to the response [Kausel and Roesset(1992)].

#### 5 Numerical examples

All the cases presented refer to a channel, 20.0m deep as illustrated in Fig. 2. Simulation analyses were performed when two rigid, circular, cylindrical cavities, placed inside this channel, are illuminated by an incident pressure load defined by the dilatational point load, expressed as in Eq.1. The two cavities are defined by their radii:  $R = 0.0m$ , 1.0m and 4.0m. The size of one cavity remains constant ( $R = 4.0m$ ) while the size of the other, placed in its vicinity, changes. Fig. 2 displays the geometry of the cross-section of the inclusions. At time  $t = 0.0$ , the channel is struck on its rigid surface by a pressure source, placed below the inclusions, on the channel's flat floor, at the origin of the coordinate system (source 1) or at  $x = 25.0m$  (source 2). Each source creates a spherical pressure pulse that propagates away from its origin. The field generated is computed at 41 receivers, spaced at equal intervals (2.0m) along the  $x$  direction. The pressure wave propagation velocity of 1500m/s, and a host fluid density of  $\rho = 1000Kg/m^3$  remain constant for all the analyses.

The computations are performed in the frequency range 4 to 512Hz, with a frequency increment of 4.0Hz, which determines the total time ( $T = 250.0ms$ ) taken for the analysis in the time domain. The source time dependence is a Ricker wavelet with a characteristic frequency of 200Hz.

The cavities are modeled with boundary elements, the number of which changes with the frequency of excitation of the harmonic load. The ratio of the wavelength of the incident waves to length of the boundary elements is kept to a minimum of 8.0. The minimum number of boundary elements used to model each cavity is never less than 30.

Simulations are performed following waves with differ-

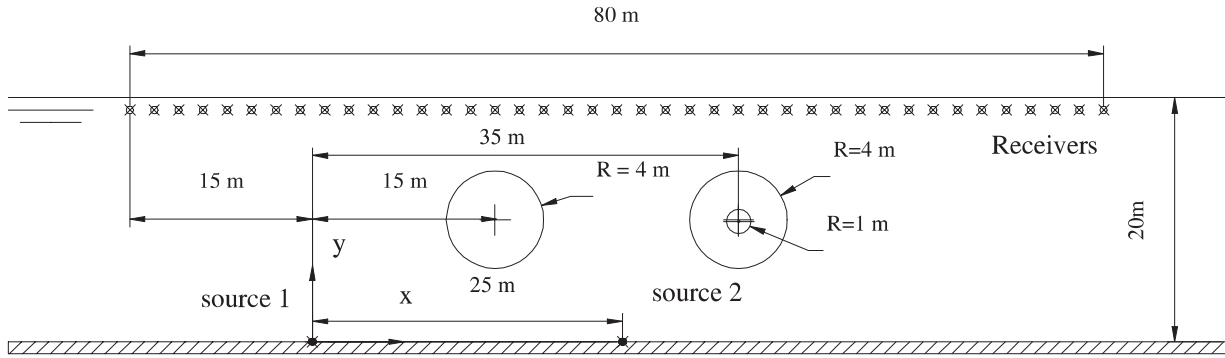


**Figure 2 :** Geometry of the channel and location of sources and receivers.

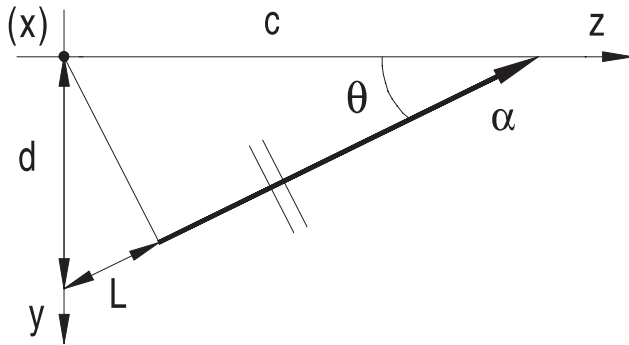


**Figure 3 :** Apparent wave velocity.

ent apparent wave velocities along the  $z$  axis, to quantitatively study the 3D effects of the scattering. This apparent wave velocity ( $c$ ) results from waves arriving at the  $z$  axis, with a path inclination given by  $\arccos(\alpha/c)$ , where  $\alpha$  is the true wave velocity (see Fig. 3). So, in the equations presented above  $k_z$  is taken to be  $\omega/c$ . In the examples selected, three apparent velocities ( $c$ ) are chosen, namely  $c = \infty m/s$ ,  $c = 3000m/s$  and  $c = 1732.05m/s$ .  $c = \infty m/s$  corresponds to waves arriving at the receivers with a  $90^\circ$  inclination in relation to the  $z$  axis, which can be understood as a pure two dimensional problem where the source is linear. As the path inclination ranges from  $90^\circ$  to  $0^\circ$ , there is a lower bound value for  $c$ , which corresponds to the slowest wave velocities  $c = 1500.0m/s$ . Below this value, there are inhomogeneous waves, which decay very rapidly with decreasing values of  $c$ . Thus,  $c = 3000m/s$  and  $c = 1732.05m/s$  correspond to waves arriving at the receivers with  $60^\circ$  and  $30^\circ$  inclination in relation to the  $z$  axis, respectively.

Fig. 4a and 4b display the time and space-frequency (Fourier amplitude spectra) response recorded at the line of receivers, inside a channel free of any inclusion, when the medium is illuminated by the point source 1, for different apparent wave velocities. These plots use a gray scale where lighter and darker shades are ascribed to positive and negative values respectively. Fig. 4a illustrates the response for  $c = \infty m/s$ . The first train of pulses in these figures represents direct incident pulses. These are followed by progressively lower amplitude pulses, which are caused by reflections between the surface and the floor of the channel. A phase shift ( $180^\circ$ ) occurs each time a pulse hits the surface, while no phase change is observed when it impinges on the rigid floor. As these pulses travel back and forth between the surface and the floor of the channel, they lose energy to the surrounding medium, and dissipate. It is further observed that the wave-front of these train pulses becomes flatter for higher order reflections.

The Fourier amplitude spectra  $[0 - 256Hz]$  of these responses exhibit pronounced peaks, caused by interference among reflections, which occur at well-defined frequencies. It can be demonstrated that the distance in frequency between successive peaks is equal to  $\Delta f = \alpha/\Delta s$ , in which  $\Delta s$  is the different path taken by successive reflections ( $\Delta s \approx 2h$ , where  $h$  is the depth of the channel), which leads to  $\Delta f \approx 37.5Hz$ . The position of the first peak is defined by the type of boundary. Since the normal propagating velocity at the base of the channel is null, the first peak occurs at  $f_0 \approx \alpha/4h \approx 18.75Hz$ .

As the apparent velocity decreases, both the arrival

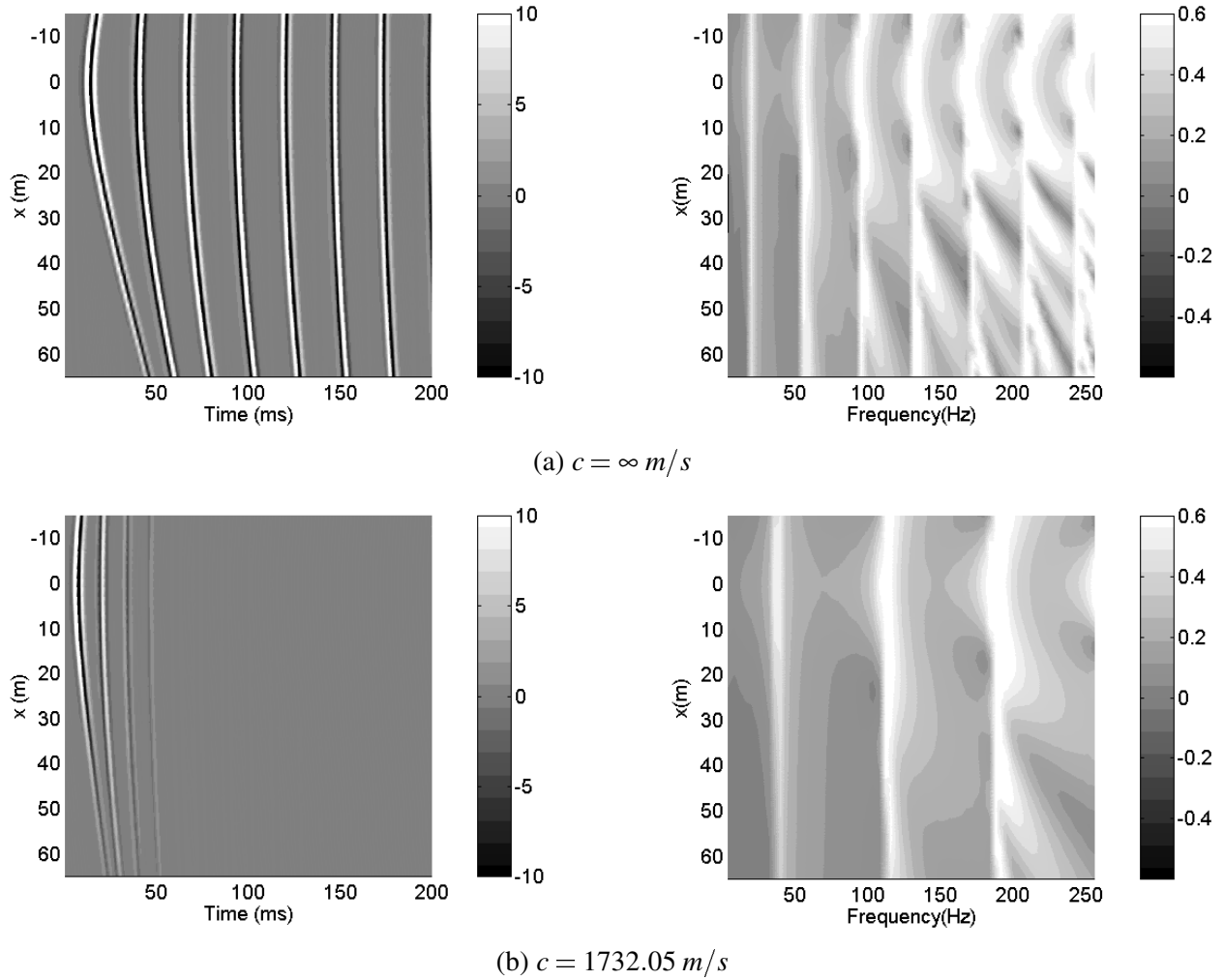


**Figure 4 :** Total time and frequency responses inside a channel free of any inclusion when Source 1 is excited.

times of the different pulses and their amplitude decrease rapidly with time. Fig. 4b illustrates this behavior when the apparent wave velocity is assumed to be  $c = 1732.05m/s$ . A pulse in these plots, with a travel time  $\tau$ , corresponds to waves that travel from the source to the reflector and back to the receiver, along a ray path with the same inclination in relation to the  $z$  axis. The travel distance ( $L$ ) in this domain is smaller because it corresponds to the projection of the initial vertical path ( $d$ ) to the inclined path, leading to a distance  $L = d \sin[\arccos(\alpha/c)]$  (see Fig. 3). In this way, the pronounced drop in the response with time as the apparent velocity decreases, indicates that the scattering energy, as the pulses travel back and forth between the surface

and the floor of the channel, is mainly concentrated along plane wave-fronts, perpendicular to the  $z$  plane. The distance in frequency between successive peaks is now equal to  $\Delta f \approx \alpha / (40.0 \sin(30^\circ)) \approx 75.0Hz$ , with the first peak occurring at  $f_0 \approx 37.5Hz$ .

Fig. 5-7 depicts the total time pressure field when two rigid cavities are submerged and subjected to the incident pressure field created by load 1. The first cavity remains constant ( $R = 4.0m$ ), and a second cavity assumes three different sizes ( $R = 0.0m, 1.0m$  and  $4.0m$ ). In these plots,  $c$  changes from  $\infty$  to  $1732.05 m/s$ .

The first wave arrivals observed in Fig. 5 show the time responses when  $c = \infty m/s$ . When only one cavity is

present the resulting field corresponds to the incident waves followed by wave trains that are directly reflected by the cavity. These are succeeded by pulses of progressively lower amplitude, which result from reverberations between the cavity and the boundaries of the channel. The field is therefore more complex than the one found for the simple channel, described earlier. However, it is still possible to identify pulses that are the result of reflections at both the surface and the floor, especially as time increases, and at receivers placed away from the cavity. The time arrivals of these pulses agree with those found for the simple channel.

Analysis of the results reveals a very small wave-field in the axis position of the cavity (a solid line is added to the plots to identify this axis). Indeed, the receivers placed close to the cavity show smaller amplitudes than do the receivers that are further away. This phenomenon is explained by the reflective power of the convex shape of the cavity, which enables energy to be reflected to the sides, away from the central zone, where the cavity is located. This behavior is even more pronounced as the time progresses, with the wave-front becoming flatter and parallel to the boundaries of the channel, as explained before. The signals recorded by the receivers furthest away from the source suffer from the so-called “shadow effect”, caused by the cavity. As a result, the amplitudes of these pulses show a strongly marked decrease behind the cavity.

The presence of a second cavity further disturbs the wave field owing to the interaction of the multiple reflections between the inclusions and the boundaries of the channel. When the second cavity has a radius of  $4.0\text{ m}$ , the resulting pressure field clearly denotes a strong interaction between the cavities. The bigger amplitude of the pulses at the receivers placed between these cavities bears witness to this behavior. In addition, the existence of waves trapped between the inclusions is observed to cause pronounced reflections at both the surface and the floor of the channel. The positions of the cavities are again identifiable by the small wave-field observed at the receivers placed above the inclusions. The “shadow effect” produced by the presence of the cavities is now more intense. The response calculated for the situation where there is a second cavity of radius  $1.0\text{ m}$  has similar wave patterns. However, while the position of the first cavity (radius  $4.0\text{ m}$ ) is easily detected in the time domain, the second cavity would require a higher excitation frequency (not

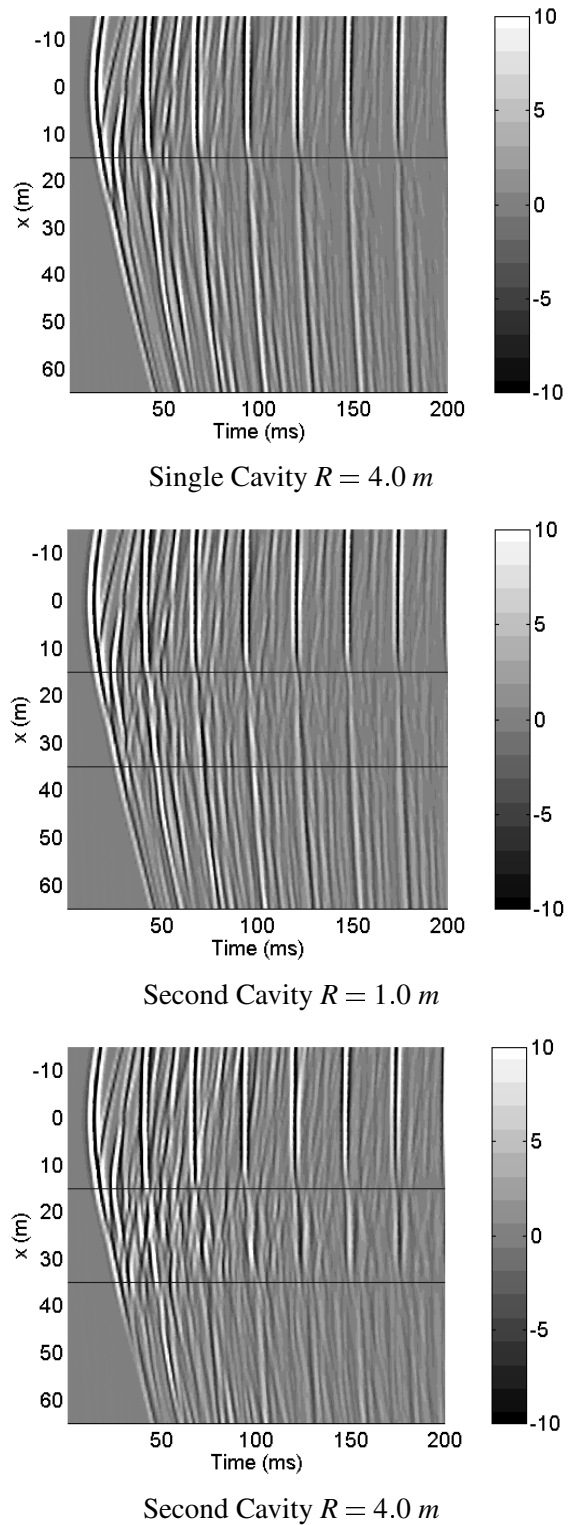
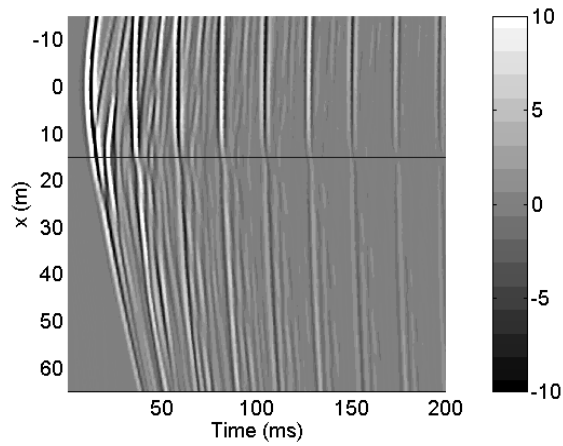
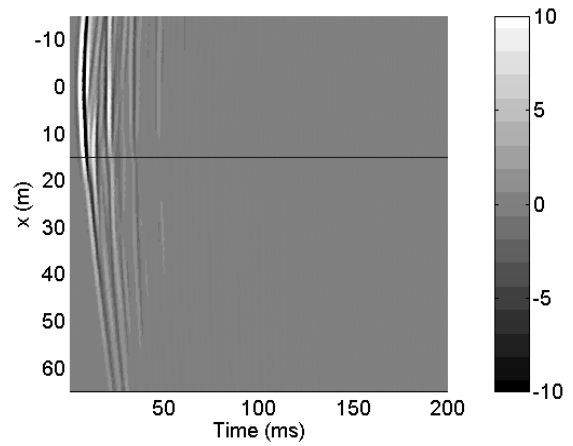


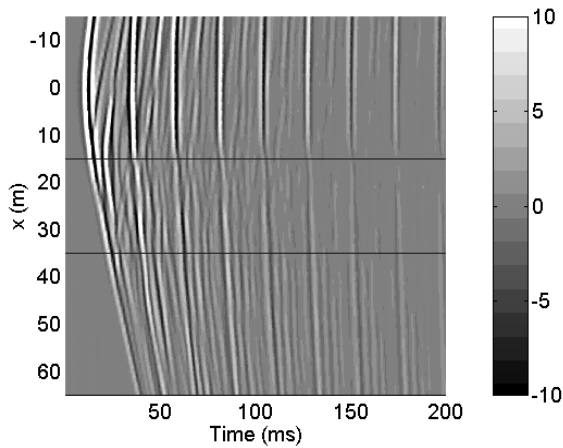
**Figure 5 :** Total time response inside a channel with submerged pipelines when Source 1 is excited:  $c = \infty\text{ m/s}$ .



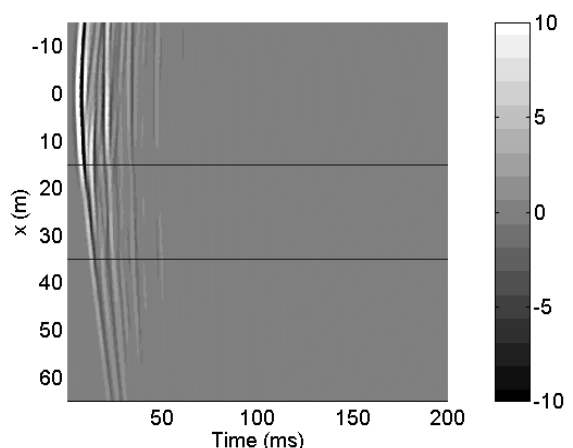
Single Cavity  $R = 4.0\ m$



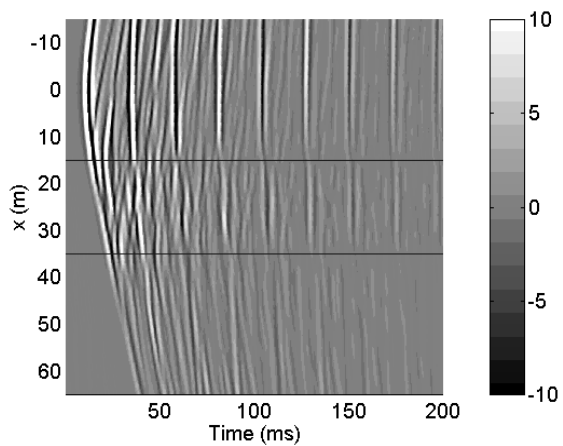
Single Cavity  $R = 4.0\ m$



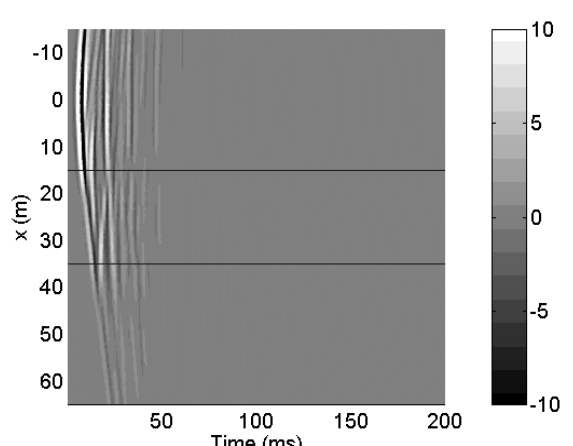
Second Cavity  $R = 1.0\ m$



Second Cavity  $R = 1.0\ m$



Second Cavity  $R = 4.0\ m$



Second Cavity  $R = 4.0\ m$

**Figure 6 :** Total time response inside a channel with submerged pipelines when Source 1 is excited:  $c = 3000\ m/s$ .

**Figure 7 :** Total time response inside a channel with submerged pipelines when Source 1 is excited:  $c = 1732.05\ m/s$ .

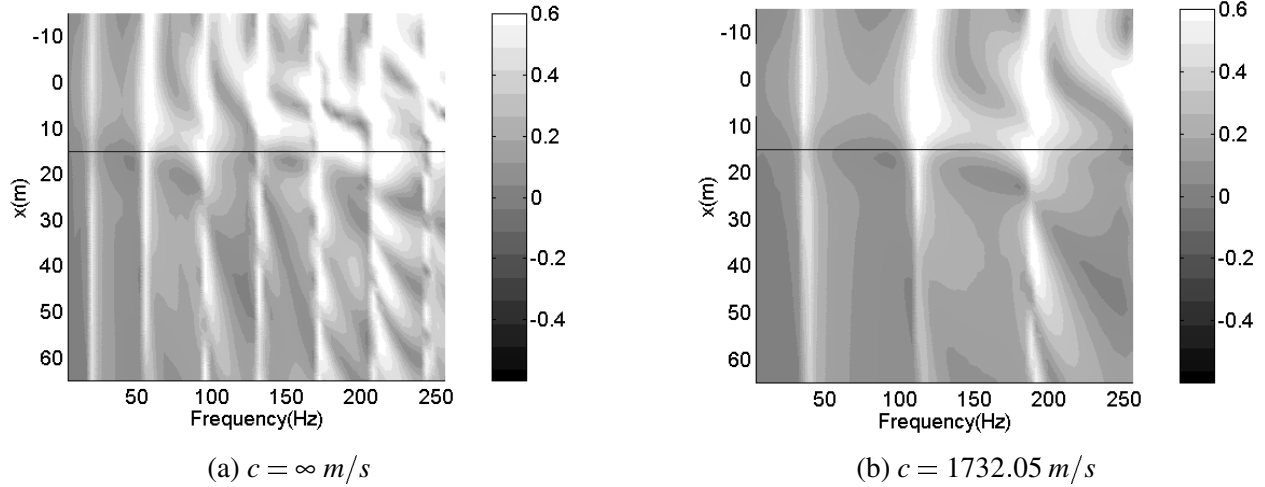


**Figure 8 :** Fourier amplitude spectra responses inside a channel with a single inclusion ( $R = 4.0 \text{ m}$ ) when Source 1 is excited.

illustrated). The “shadow” created is similar to the one produced where there is a single cavity.

As the apparent velocity decreases (Fig. 6 and 7), the behavior of the responses is similar to that found for the channel in the absence of any inclusion, with a pronounced drop in the response as time progresses. The main features observed for  $c = \infty \text{ m/s}$  are still apparent: a very small wave-field at receivers placed directly above the cavity, more noticeable as time progresses; the presence of a “shadow effect” caused by the cavities; the resulting pressure field clearly denoting a strong interaction between the cavities; the existence of waves trapped between the inclusions. However, when the apparent velocity reaches low values, such as  $c = 1732.05 \text{ m/s}$ , the definition of the position of the cavities in the time responses is more difficult because of the earlier decrease of the response. This behavior even holds when there are two large inclusions ( $R = 4.0 \text{ m}$ ) present. The “shadow” creation becomes the only identifiable surviving effect when the apparent velocity is very low.

The main features observed for  $c = \infty \text{ m/s}$  are still apparent: a very small wave-field at receivers placed directly above the cavity, more noticeable as time progresses; the presence of a “shadow effect” caused by the cavities; the resulting pressure field clearly denoting a strong interaction between the cavities; the existence of waves trapped between the inclusions. However, when the apparent ve-

locity reaches low values, such as  $c = 1732.05 \text{ m/s}$ , the definition of the position of the cavities in the time responses is more difficult because of the earlier decrease of the response. This behavior even holds when there are two large inclusions ( $R = 4.0 \text{ m}$ ) present. The “shadow” creation becomes the only identifiable surviving effect when the apparent velocity is very low.

Fig. 8a illustrate the Fourier amplitude spectra response when a single cavity is present for an apparent wave velocity  $c = \infty \text{ m/s}$ . Lower amplitude responses are found at receivers placed behind the inclusion. In addition, peaks of response related to the depth and type of boundaries of the channel are observed, as in the absence of a cavity. This phenomenon is more evident for receivers subjected to the shadow effect produced by the cavity. Similar conclusions can be drawn from an analysis of the Fourier spectra when the apparent wave velocity is set to  $c = 1732.05 \text{ m/s}$  (see Fig. 8b).

Fig. 9 illustrates the response obtained when the submerged cavities are illuminated by the second load, for an apparent wave velocity of  $c = 3000 \text{ m/s}$ . The wave field produced by the reverberations on both cavities is enhanced, as the higher amplitude of the pulses at receivers placed between cavities shows, even for later times.

The “shadow” produced when two equal-sized cavities are placed side by side inside the channel is symmetric

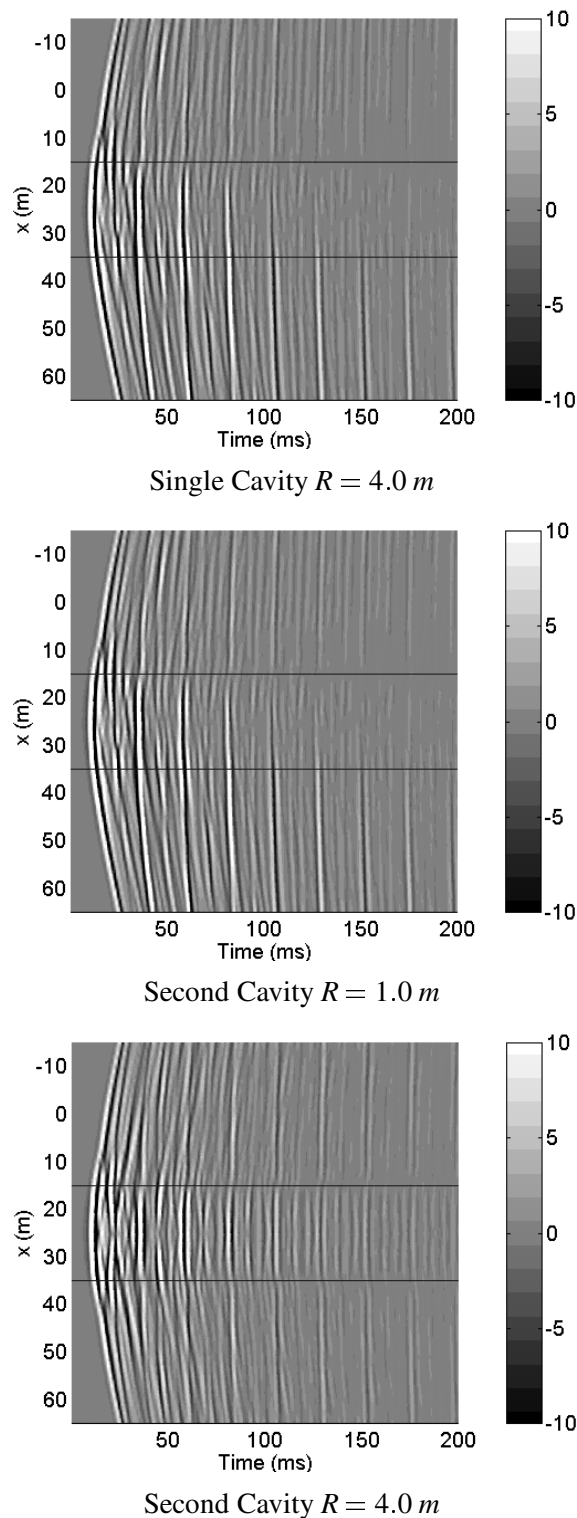


**Figure 9** : Total time responses when Source 2 is excited:  $c = 3000 \text{ m/s}$ .

in relation to the source. However, when one cavity is smaller, the shadow effect behind this second cavity loses importance, whereas it becomes even more pronounced behind the first, larger, cavity. This is because the smaller size of the second cavity results in the wave-field created between cavities being smaller.

To access the position of the cavities, the total pressure field is analyzed in space-frequency  $(x, f)$  domains when low frequency harmonic excitation loads placed at position 1 are used (1.0; 50.0 Hz). First, the total field difference generated when the single cavity ( $R = 4.0 \text{ m}$ ) or the two large cavities ( $R = 4.0 \text{ m}$ ) are inserted in the fluid channel is presented in Fig. 10, for apparent wave velocities of  $c = \infty \text{ m/s}$  (Fig. 10a) and  $c = 1732.05 \text{ m/s}$  (Fig. 10b).

Our results show that when one cavity is present the larger differences appear in the vicinity of the axis of the inclusion, allowing its position to be detected. As the apparent velocity, decreases the amplitude of the pressure field difference diminishes, but it still enables the position of the inclusion to be located. When two cavities are present, the amplitude of the pressure field difference is intense in the vicinity of both cavity axes, allowing the identification of their position. Again, as the apparent velocity changes from  $c = \infty \text{ m/s}$  to  $c = 1732.05 \text{ m/s}$ , the field difference decreases, but the positions of both cavities remain detectable.

Next, the total field difference generated when a second cavity is inserted in the fluid channel hosting a former cavity ( $R = 4.0 \text{ m}$ ) is displayed in Fig. 11. The results are presented for two apparent wave velocities,  $c = \infty \text{ m/s}$  (Fig. 11a) and  $c = 1732.05 \text{ m/s}$  (Fig. 11b), for second cavities of radius  $R = 1.0 \text{ m}$  and  $R = 4.0 \text{ m}$ . In these plots, the presence of the second cavity is clearly visible, even when the second cavity has a small radius. As we move to lower apparent wave velocities the main features found before are maintained: the field difference is smaller, but is again located in the vicinity of the second cavity axis.

The field generated inside a fluid channel when illuminated by lower harmonic frequency pressure loads is highly dependent on the thickness of the fluid channel. It places the first peaks of response in the Fourier spectra at frequencies relating the depth of the channel and its boundary types, independently of the position of the source and receivers. When a rigid cavity is inserted inside the fluid channel the field generated by those low

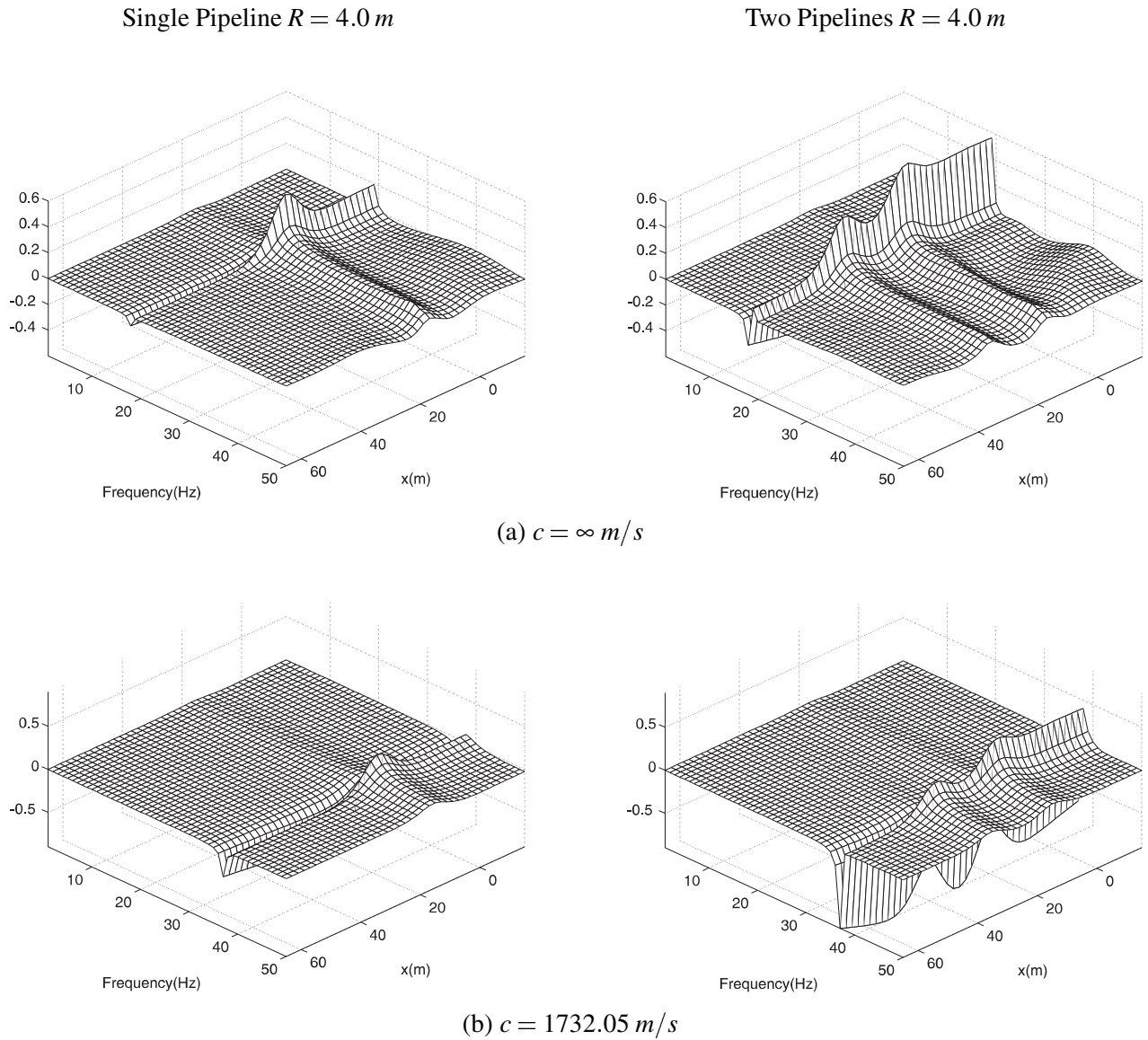


**Figure 10** : Fourier amplitude spectra difference in the fluid channel generated when pipelines are inserted in the presence of Source 1.

frequency harmonic loads is only slightly modified in its vicinity. Indeed, low frequency waves, given their long wave-lengths, are not easily disturbed by the presence of a relatively small inclusion. The field generated is therefore only changed at receivers directly above the inserted inclusion, trying to reproduce its depth. Given the curved boundary of the inclusion, and the long wave-lengths of the waves excited, the definition of its depth is not perfect, resulting in a masked field for a broad

range of frequencies. This phenomenon explains the detection of the inclusions described above. Notice, that at frequencies related to the depth of the channel  $f_0 \approx [\alpha/(2h \sin(\theta))]/2$ , the wavefield is modified as a consequence of the reflective power of the convex boundary of the inclusions. Indeed, at these frequencies, the Fourier amplitude spectra difference is modified less at receivers placed behind the pipelines, where the shadow effect exists, while it appears more pronounced at receivers placed

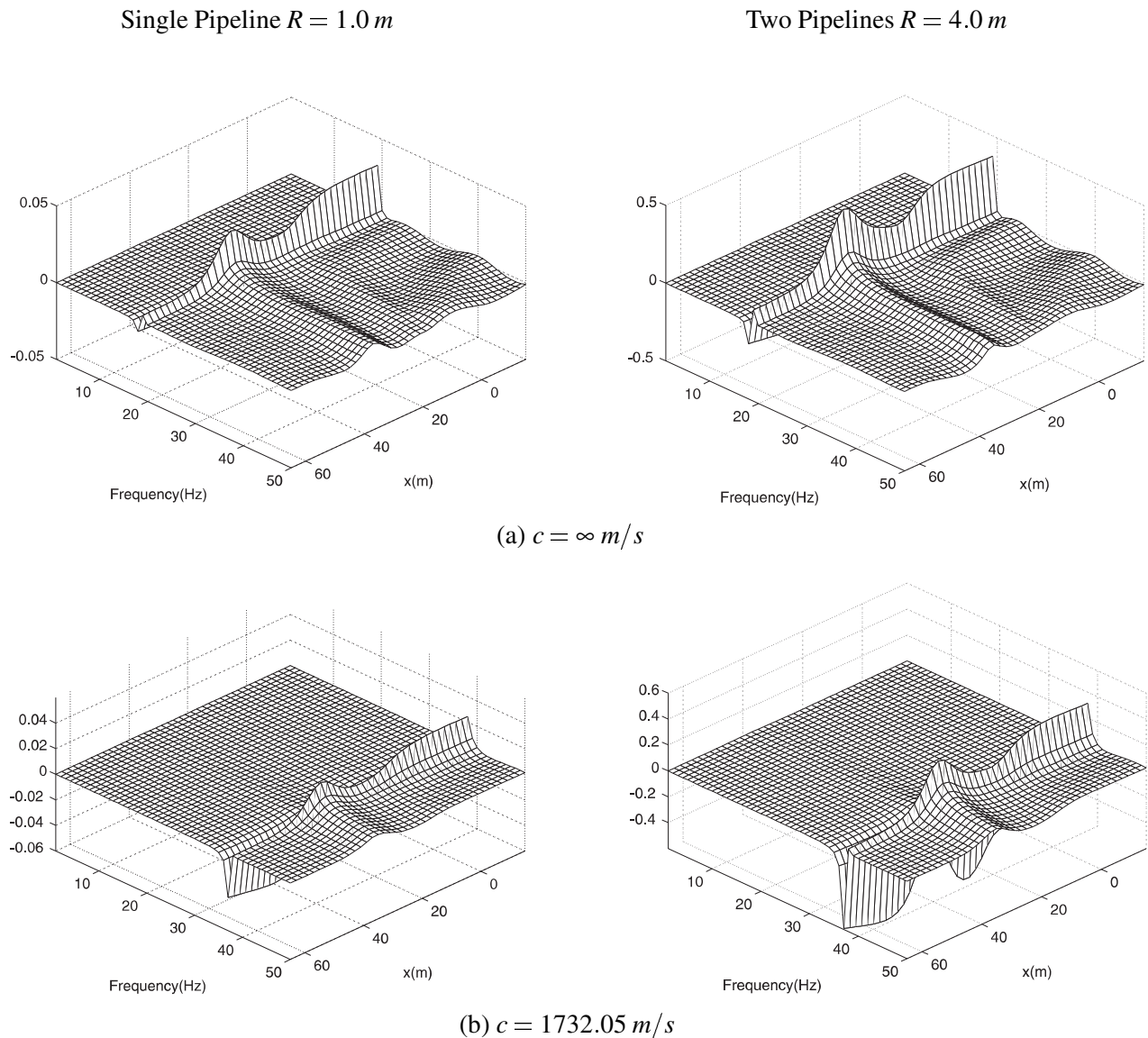


**Figure 11** : Fourier amplitude spectra difference generated when a second inclusion is inserted in the fluid channel hosting a former cavity ( $R = 4.0\text{ m}$ ) in the presence of Source 1.

closer to the source, where the waves directly reflected by the inclusions are added (see Fig. 10 and 11).

## 6 Conclusions

A boundary element formulation was used to evaluate the 3D scattered field generated by a dilatational point load illuminating circular cylindrical rigid cavities placed inside a fluid channel. Validation of the method has been presented, showing a very good agreement with results

obtained by analytical solutions.

Simulation analyses performed for the case when rigid, circular, cylindrical cavities are placed inside a fluid channel allowed the authors to evaluate the influence of submerged objects in the acoustic wavefield generated by a dilatational load placed at its floor. Results for different apparent velocities were obtained in both the frequency and time domain.

When a single cavity was placed inside the channel, anal-

ysis of the results in the time domain reveals a very small wave-field at receivers placed above its axis, distinctly showing the existence of a submerged object. In addition, a significant decrease in the amplitude was observed behind the cavity. The same conclusion can be drawn for the case of two large cylindrical cavities, allowing clear identification of their presence. For lower apparent velocities, the response exhibited similar features, although the amplitude of the response decayed sooner in time.

Frequency domain results were also obtained, showing that both the depth and the type of boundaries of the channel could be accessed by looking at the position of amplitude peaks. Analysis of the response demonstrated that the presence of the cavities could be easily detected at low frequencies. It was further concluded that even for a comparatively small second cavity, the total pressure field difference, generated by its insertion in the fluid channel, exhibited a clearly visible amplitude peak at receivers placed above its axis, which permitted the presence of a second object to be detected. The method used here was found to be efficient, yielding good results and enabling the position of submerged objects to be correctly identified.

## References

- Ahluwalia, D. S.; Keller, J. B.** (1977): Exact and asymptotic representations of the sound field in a stratified ocean, In *Wave Propagation and Underwater Acoustics*, J.B.Keller and J.S. Papadakis (eds), Springer, New York, pp. 14-85.
- Bouchon, M.; Keiti Aki** (1977): Discrete wave-number representation of seismic source wavefields, *Bull. Seism. Am.*, vol. 67, pp. 259-277.
- Claerbout, J.F.** (1976): Fundamentals of geophysical data processing, McGraw-Hill.
- Cordier, Jean-Pierre** (1985): Velocities in reflection Seismology, D. Reidel Publishing Company, Holland.
- Dawson, T. W.; Fawcett, J. A.** (1990): A boundary integral equation method for acoustic scattering in a waveguide with nonplanar surfaces, *J. Acoust. Soc. Am.*, vol. 87, pp. 1110-1125.
- Fawcett, J. A.** (1996a): The computation of the scattered pressure field from a cylinder embedded between two half-spaces with different densities, *J. Acoust. Soc. Am.*, vol. 99, pp. 2435-2438.
- Fawcett, J. A.** (1996b): Acoustic scattering from cylindrical objects embedded between two half-spaces, *J. Acoust. Soc. Am.*, vol. 100, pp. 3053-3060.
- Godkin, Carl B.** (1985): Travel time inversion of multi-offset vertical seismic profiles, *Master Thesis*, Massachusetts Institute of Technology, Cambridge, Massachusetts, USA.
- Griffiths, D. H.; King, R. F.** (1981): Applied geophysics for geologists and engineers, Pergamon Press, pp. 1-69.
- Kausel, E.; Roesset, J. M.** (1992): Frequency domain analysis of undamped systems, *Journal of Engineering Mechanics*, ASCE; vol. 118, no. 4, pp. 721-734.
- Manolis, G. D.; Beskos, D. E.** (1988): Boundary Element Methods in Elastodynamics, Unwin Hyman (sold to Chapman and Hall), London.
- Özdoğan, Yilmaz** (1987): Seismic data processing, SEG Press.
- Pao, Y. H.; Mow, C. C.** (1973): Diffraction of Elastic Waves and Dynamic Stress Concentrations, Crane and Russak.
- Tadeu, A.** (1992): Modelling and seismic imaging of buried structures, *PhD Thesis*, M.I.T., Department of Civil Engineering, Cambridge, Massachusetts.
- Tadeu, A.; Godinho, L.** (1999): 3D wave scattering by a fixed cylindrical inclusion submerged in a fluid medium, *Engineering. Analysis Boundary Elements*, vol. 23, pp. 745-756.

